The Star Formation Newsletter #344 18-22

東大M2 森井嘉穂

18. An orbital release model for the Orion BN/KL fingers

19. A Core Mass Function Indistinguishable from the Salpeter Stellar Initial Mass Function Using 1000 au Resolution ALMA Observations

20. Optical Properties of Interstellar Dust around the Orion A Molecular Cloud

21. Probing Protoplanetary Disk Winds with C II Absorption

22. TIMES II: Investigating the Relation Between Turbulence and Star-forming Environments in Molecular Clouds

19. A Core Mass Function Indistinguishable from the Salpeter Stellar Initial Mass Function Using 1000 au Resolution ALMA Observations

Genaro Suárez, Roberto Galván-Madrid, Luis Aguilar, Adam Ginsburg, Sundar Srinivasan, Hauyu Baobab Liu, Carlos G. Román-Zúñiga

We present the core mass function (CMF) of the massive star-forming clump G33.92+0.11 using 1.3 mm observations obtained with the Atacama Large Millimeter/submillimeter Array (ALMA). With a resolution of 1000 au, this is one of the highest resolution CMF measurements to date. The CMF is corrected by flux and number incompleteness to obtain a sample that is complete for gas masses $M \gtrsim 2.0\ M_{\odot}$. The resulting CMF is well represented by a power-law function ($dN/d\log M \propto M^{\Gamma}$), whose slope is determined using two different approaches: *i*) by least-squares fitting of power-law functions to the flux- and number-corrected CMF, and *ii*) by comparing the observed CMF to simulated samples with similar incompleteness. We provide a prescription to quantify and correct a flattening bias affecting the slope fits in the first approach, which is caused by small-sample or edge effects when the data is represented by either classical histograms or a kernel density estimate, respectively. The resulting slopes from both approaches are in good agreement each other, with $\Gamma = -1.11^{+0.12}_{-0.11}$ being our adopted value. Although this slope appears to be slightly flatter than the Salpeter slope $\Gamma = -1.35$ for the stellar initial mass function (IMF), we find from Monte Carlo simulations that the CMF in G33.92+0.11 is statistically indistinguishable from the Salpeter representation of the stellar IMF. Our results are consistent with the idea that the form of the IMF is inherited from the CMF, at least at high masses and when the latter is observed at high-enough resolution.

大質量星形成クランプG33.92+0.11のCMFをALMAで取得した1.3 mm連続波を用いて作成 (分解能1,000 au)
冪乗分布を示した
べきの決め方 i) flux- and number-corrected CMFに対して最小二乗フィッティング
ii) 同様の不完全さをもつサンプルのシミュレーションで観測したCMFを再現する
→ $M \propto M^{\Gamma}$ $(\Gamma = -1.11^{+0.12}_{-0.11})$
Salpeter IMFのべきよりも浅いが, 統計的には区別できない程度
サンプル数の少なさがべきに与える影響などを詳しく調べている

対象領域
G33.92+0.11 UC HII 領域
データ
ALMA 12m+ACA 分解能~1,000 au at 7.1 kpc
1.3 mm連続波
コアの同定
`dendrogram`
`min_value`= 5 MAD, `min_delta`=5 MAD, `min_npix`=beam size
(MAD=median absolute deviation)
→ 40 leaf (40個のコアを同定)
背景放射の除去
孤立したものは ×2 rcと×3 rc で囲まれるリング内の平均強度
階層構造をもつ場合はおおもとの構造(trunk)の平均強度

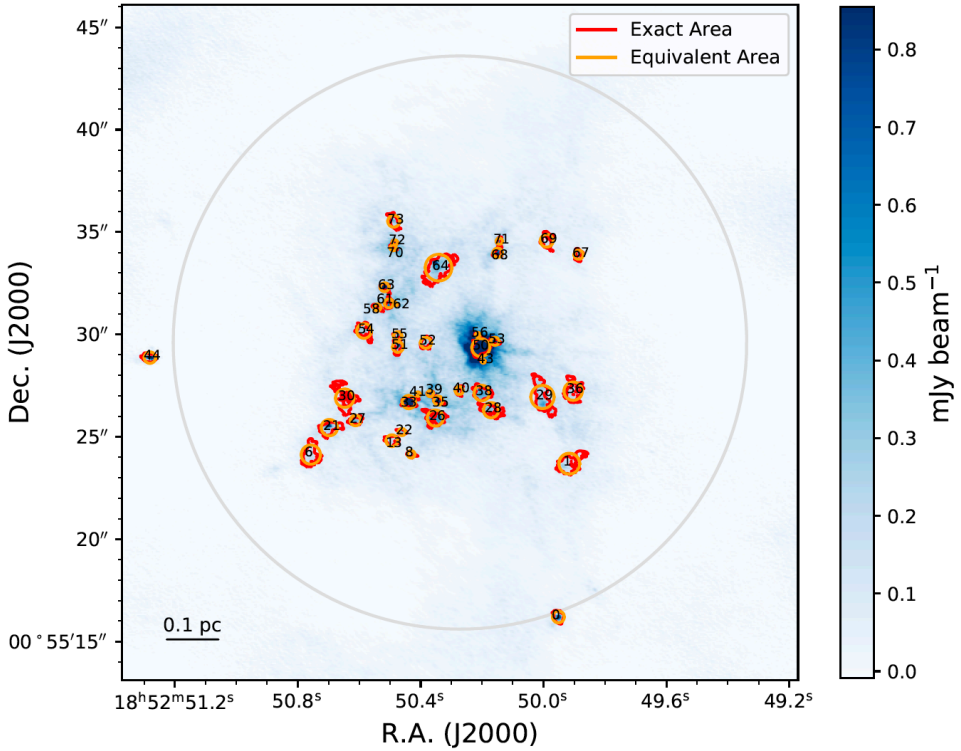

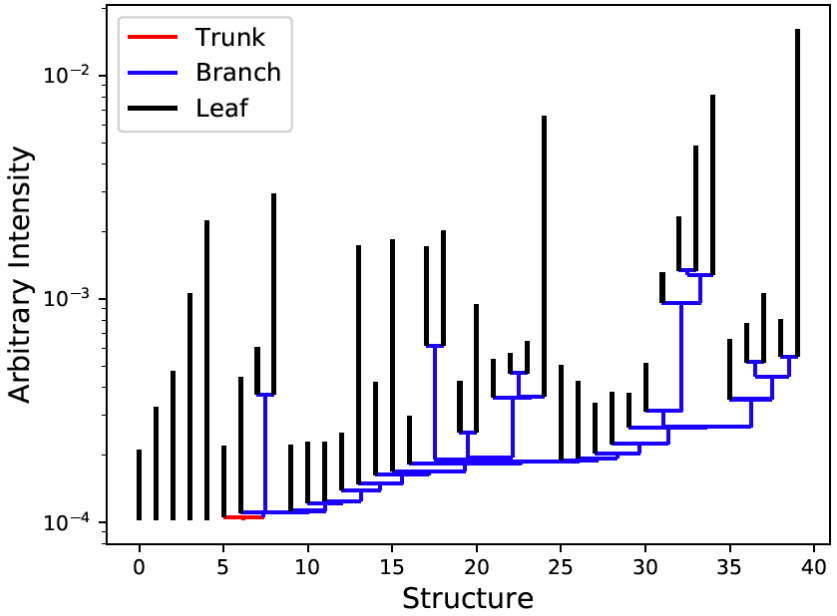

質量の見積もり

$$M_{\rm gas} = 26.6\left(e^{11.1\,{\rm K}/T_{\rm dust}} - 1\right)\left(\frac{F_{1.3\,{\rm mm}}d^2}{\kappa_{1.3\,{\rm mm}}}\right)M_\odot$$

光学的に薄いという仮定($T_{\rm B}$=0.2-5.6 K)
$d = 7.1^{+1.2}_{-1.3}$ kpc
$\kappa_{1.3\,{\rm mm}} = 0.6\ {\rm cm^2 g^{-1}}$
$T_{\rm dust}(r) = 180\times\sqrt{0.00175/r}\times\omega(r) + 25\times(1-\omega(r)),\ \omega(r) = e^{-r/0.0175}$
$r \geq 0.05$ pcでは25 K それより内側では25 K以上
ただし$r = 0$はクランプ中心
→ 0.44-59 $M_\odot$

ALMA観測による不完全さの補正

Monte Carlo simulation で楕円ガウシアンコアを10^4個生成
サイズ, 質量, クランプ内の位置をランダムに設定
10個ずつ観測データに混ぜてastrodendroを実行

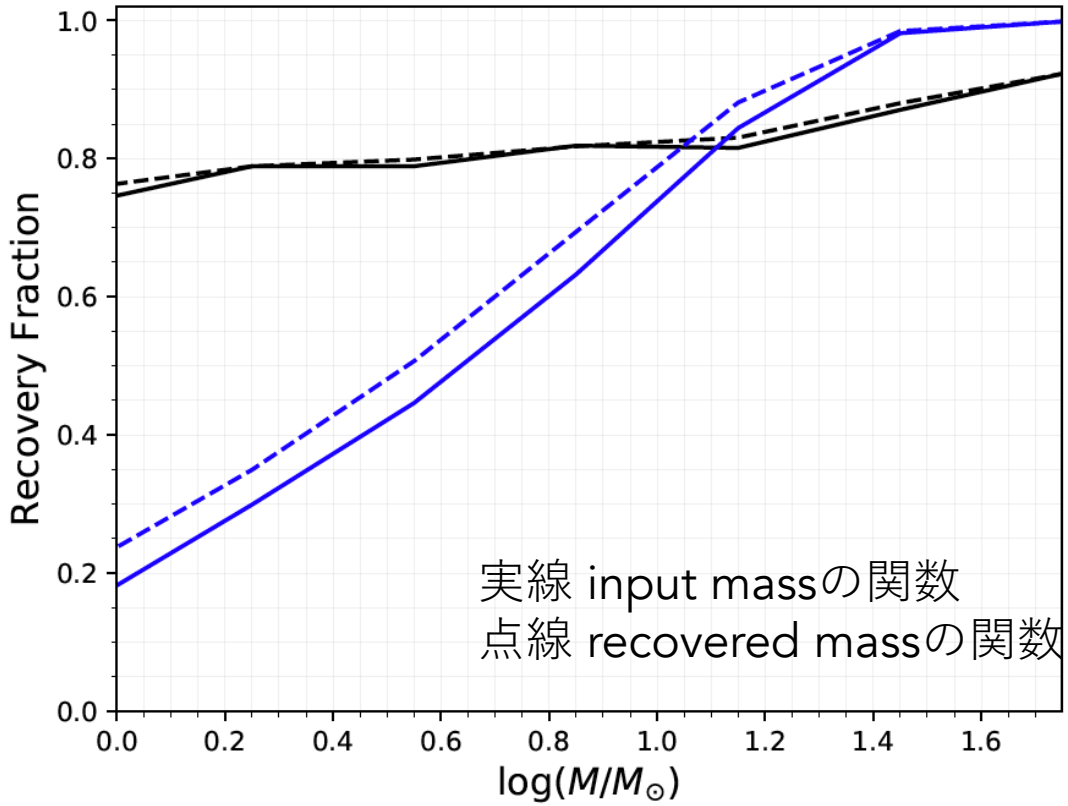

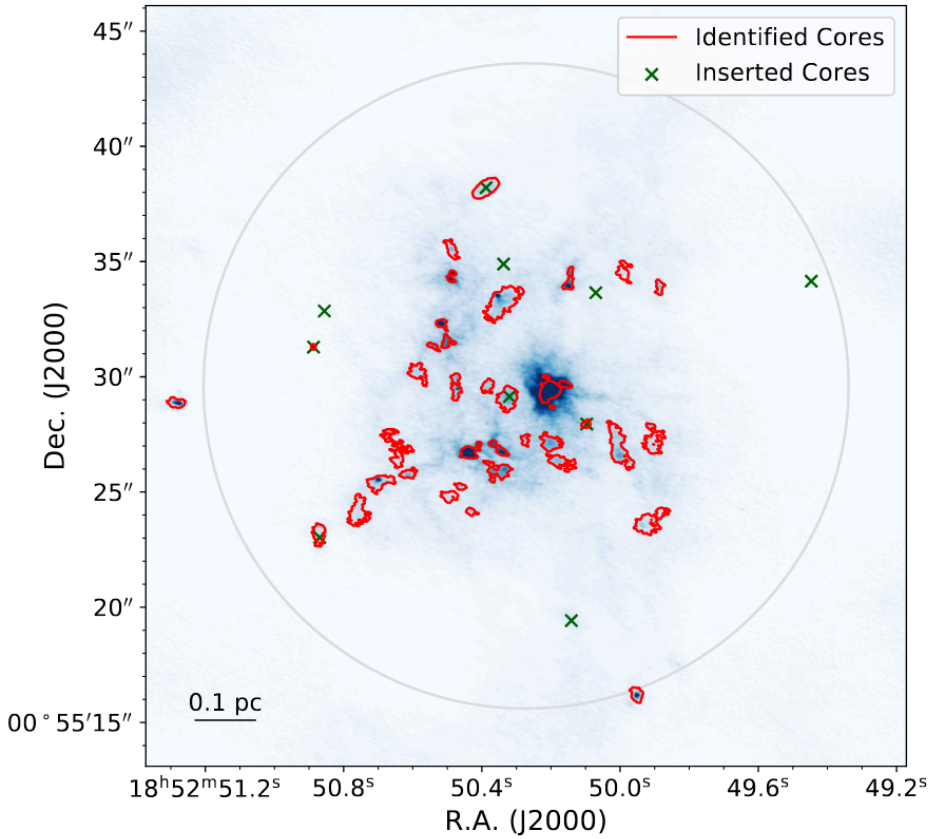

f_{flux} inputに対するoutputのflux比の中央値 (黒)
f_{num} 加えたコアの数に対する同定されたコアの個数比の中央値 (青)

べきの求め方1 フラックスや数を補正してフィット

classical histogram

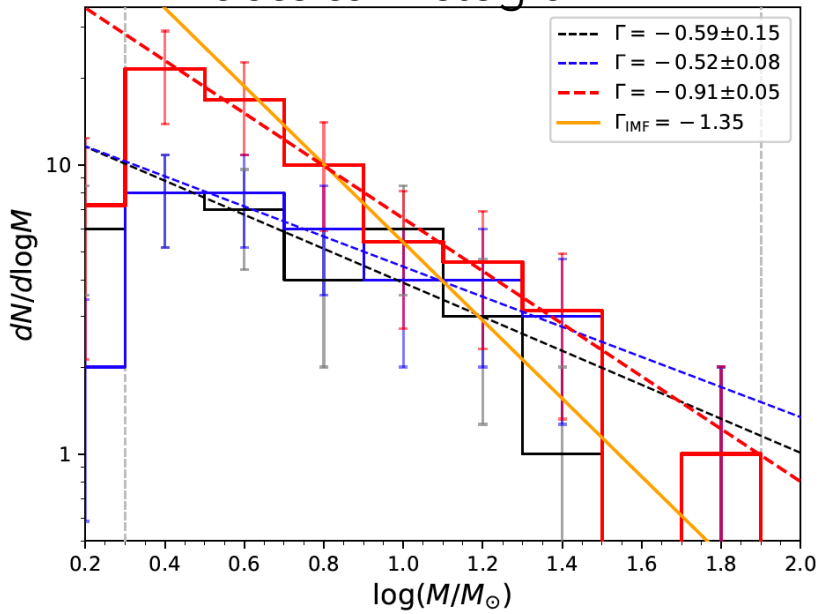

kernel density estimation (KDE)

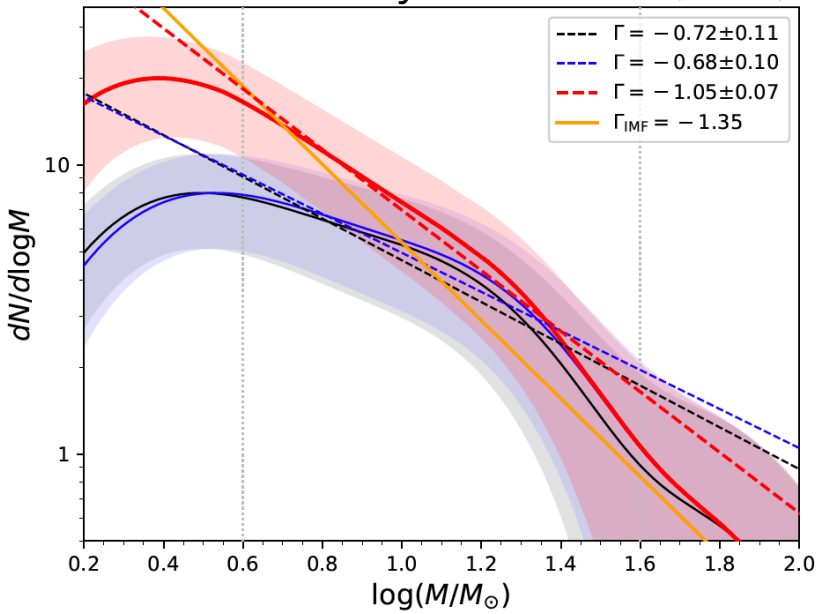

raw CMF
flux-corrected CMF
flux- and
number-corrected CMF

サンプル数の少なさによる平坦化

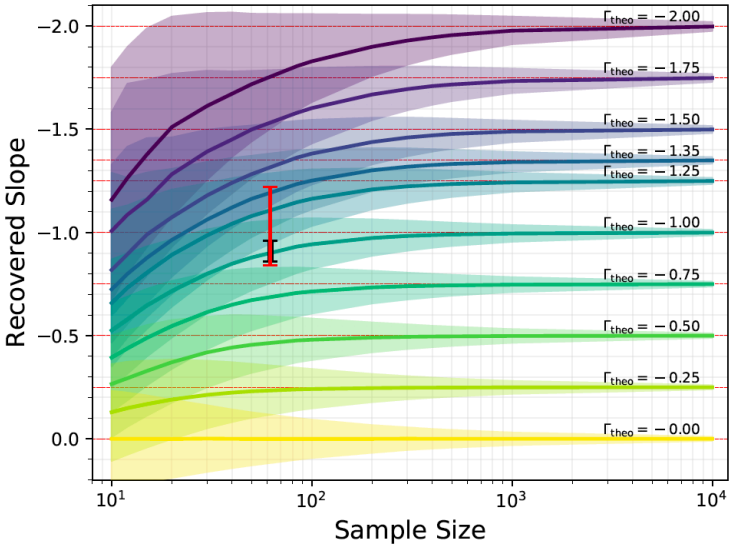

edge effectによる影響

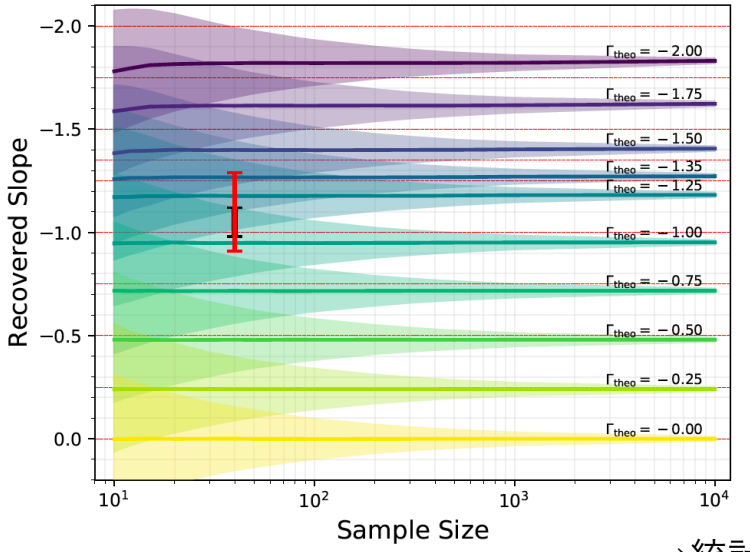

black bar corrected CMFのbest slope fit
red bar true slope (平坦化を考慮)

← -2から0のべきをもつ分布を
サンプル数10-10^4の場合で
それぞれ10^5回試行した際の中央値と
68%の信頼区間

Correction Level	$\Gamma^a_{\rm hist}$	$\Gamma^b_{\rm KDE}$
Raw[d]	-0.59±0.15	-0.72±0.11
Flux-Corrected	-0.52±0.08	-0.69±0.10
Flux- and Number-Corrected[e]	-0.91±0.05	-1.05±0.07
Inferred or *True*[f]	$-1.03^{+0.18}_{-0.20}$	$-1.10^{+0.19}_{-0.19}$

→統計的に正しいべきを求められていないことを示唆

べきの求め方2 シミュレーションと比較

-2から0まで(0.01刻み)のべきをもつべき乗分布のサンプルを用意(サンプル数30) 0.3< log($M/M_\odot$)<1.9

f_{flux}をかけて質量(flux)を補正
補正した質量を使ってf_{num}を計算し0から1の乱数と比較　乱数の方が小さい場合その質量はkeep, 大きい場合はreject
(観測でその質量のコアが検出される確率をここで考慮)
各分布に対して30個分の質量が得られるまで実行
raw CMFとシミュレートしたものにKS testを適用し最もKS statisticが小さくなるべきを計算
理論的なべきのPDFを得るために10^5回計算

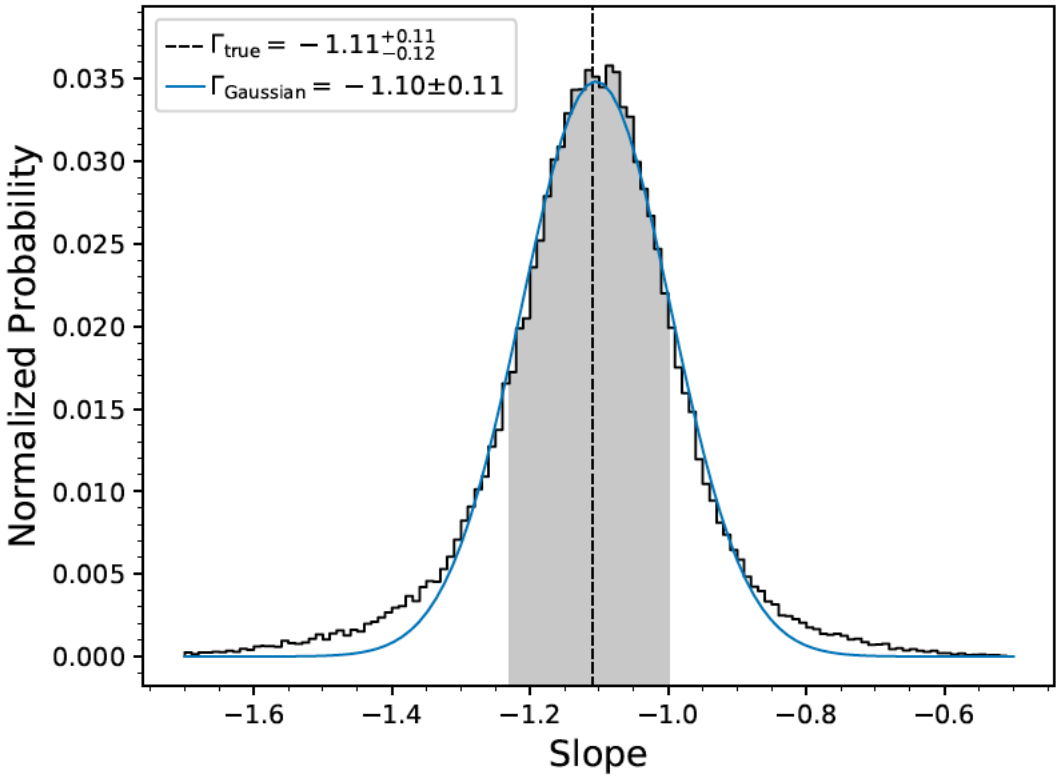

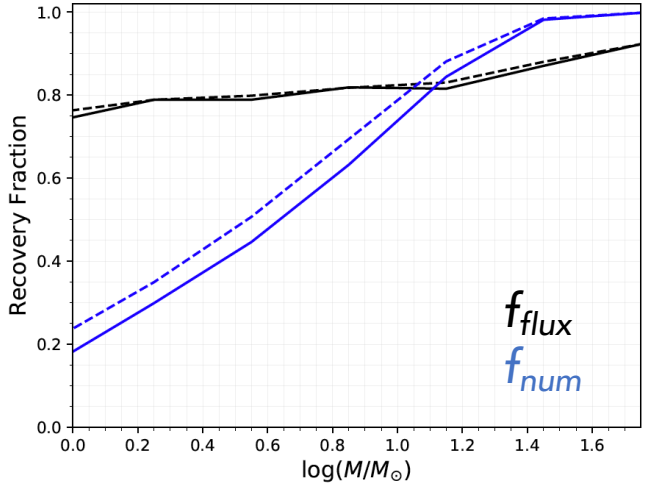

フラックスとコア数の補正係数

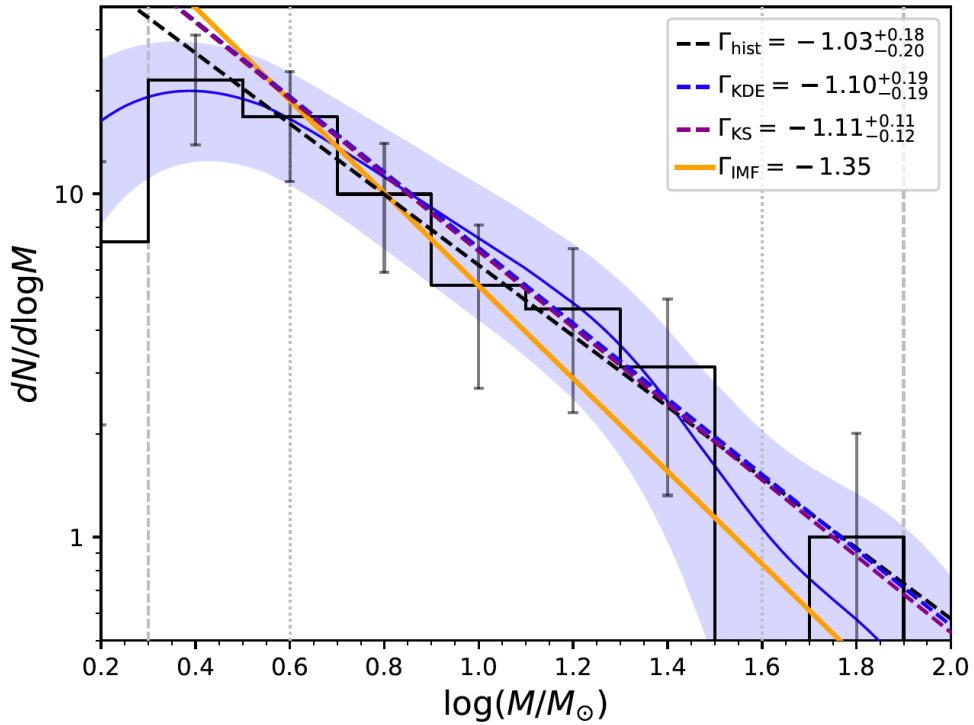

G33.92 CMFのべきはSalpeter IMFよりわずかに浅い
(星ありと星なしを分けていないから?)
が, 区別できない程度(1 σ以内で一致)

多くの大質量星形成領域で見積もられているべきと似ている

Table 3. CMFs of Diverse Star-Forming Regions Using ALMA Observations.

Region	Mass Range ($M_\odot$)	Γ	Synthesized Beam ($''\times''$)	Distance (kpc)	Resolution[a] (au)	Detection Algorithm	Reference
G33.92+0.11	> 2.0	$-1.11^{+0.12}_{-0.11}$	0.16×0.09	7.1	1000	*dendrogram*	This work
3 Clouds[b]	> 5.90	-1.04 ± 0.08	0.25×0.17	8.2	1700	*dendrogram*	Lu et al. (2020)
NGC6334	> 2	-1.10 ± 0.02	1.6×1.2	1.3	1800	`SExtractor`	Sadaghiani et al. (2020)
W43-MM1	1.6–100	-0.96 ± 0.02	0.53×0.37	5.5	2400	*getsources*	Motte et al. (2018b)
G28.37+0.07	> 0.79	-0.87 ± 0.07[c]	0.5×0.5	5	2500	*dendrogram*	Kong (2019)
G28.37+0.07	> 0.79	-1.37 ± 0.06[c]	0.5×0.5	5	2500	*astrograph*	Kong (2019)
G286.21+0.17	$\gtrsim 1$	-1.24 ± 0.17	1.07×1.02	2.5	2600	*dendrogram*	Cheng et al. (2018)
G286.21+0.17	$\gtrsim 1$	-0.64 ± 0.13	1.07×1.02	2.5	2600	*clumpfind*	Cheng et al. (2018)
28 dense clumps[d]	$\gtrsim 5.0$	-0.94 ± 0.08	$\approx 1 \times 1$[e]	2.8[e]	≈ 2800[f]	*dendrogram*	O'Neill et al. (2021)
7 IRDCs	≥ 0.79	-0.86 ± 0.11	1.36×0.82	4.4[e]	4600[f]	*dendrogram*	Liu et al. (2018)
7 IRDCs	≥ 1.26	-0.70 ± 0.13	1.36×0.82	4.4[e]	4600[f]	*dendrogram*	Liu et al. (2018)
12 IRDCs	$\gtrsim 0.6$	-1.07 ± 0.09	1.33×1.13[e]	4[e]	4900[f]	*dendrogram*	Sanhueza et al. (2019)
G305.137+0.069	> 3	0.02 ± 0.37	2.39×2.10	3.4	7600	GaussClump	Servajean et al. (2019)

22. TIMES II: Investigating the Relation Between Turbulence and Star-forming Environments in Molecular Clouds

Hyeong-Sik Yun, Jeong-Eun Lee, Neal J. Evans II, Stella S. R. Offner, Mark H. Heyer, Jungyeon Cho, Brandt A. L. Gaches, Yao-Lun Yang, How-Huan Chen, Yunhee Choi, Yong-Hee Lee, Giseon Baek, Minho Choi, Jongsoo Kim, Hyunwoo Kang, Seokho Lee, Ken'ichi Tatematsu

We investigate the effect of star formation on turbulence in the Orion A and Ophiuchus clouds using principal component analysis (PCA). We measure the properties of turbulence by applying PCA on the spectral maps in ^{13}CO, C^{18}O, HCO$^+$ J =1−0, and CS J =2−1. First, the scaling relations derived from PCA of the ^{13}CO maps show that the velocity difference (δv) for a given spatial scale (L) is the highest in the integral shaped filament (ISF) and L1688, where the most active star formation occurs in the two clouds. The δv increases with the number density and total bolometric luminosity of the protostars in the sub-regions. Second, in the ISF and L1688 regions, the δv of C^{18}O, HCO$^+$, and CS are generally higher than that of ^{13}CO, which implies that the dense gas is more turbulent than the diffuse gas in the star-forming regions; stars form in dense gas, and dynamical activities associated with star formation, such as jets and outflows, can provide energy into the surrounding gas to enhance turbulent motions.

Orion AとOphiuchusにおいて星形成が乱流に及ぼす影響を主成分分析(PCA)により調べた

^{13}CO, C^{18}O, HCO$^+$ (いずれもJ=1-0), CS (J=2-1)

^{13}COマップのPCAから導出したスケール則 $\delta v = \delta v_0 L^{\alpha}$

→δvがintegral shaped filamentでもっとも大きく, 数密度, total L_{bol}と相関あり

C^{18}O, HCO+, CSのδvが^{13}COのより一般的に大きい→dense gasの方がturbulent

mapping Turbulent properties In star-forming MolEcular clouds down to the Sonic scale (TIMES)

観測データ

13.7 m望遠鏡　Taeduk Radio Astronomy Observatory (TRAO)

Orion A, Ophiuchus

速度分解能 0.04 km s^{-1} at 110 GHz

ビームサイズ 46″ at 110 GHz

^{13}CO, C^{18}O, HCN, HCO$^+$, N_2H^+ (いずれもJ=1-0), CS (J=2-1)

主成分分析 PCA
観測したスペクトルから乱流の低次速度構造関数を導出する

$$\delta v = \delta v_0 L^{\alpha}$$

δv: 速度差 L: 空間スケール δv_0: 1 pcでの速度差

局所的なエネルギー散逸/流入(星形成活動によるフィードバック)
ビリアル, プラズマパラメーターや乱流のsolenoidal fraction
天体までの距離の不確かさ
の影響を受ける

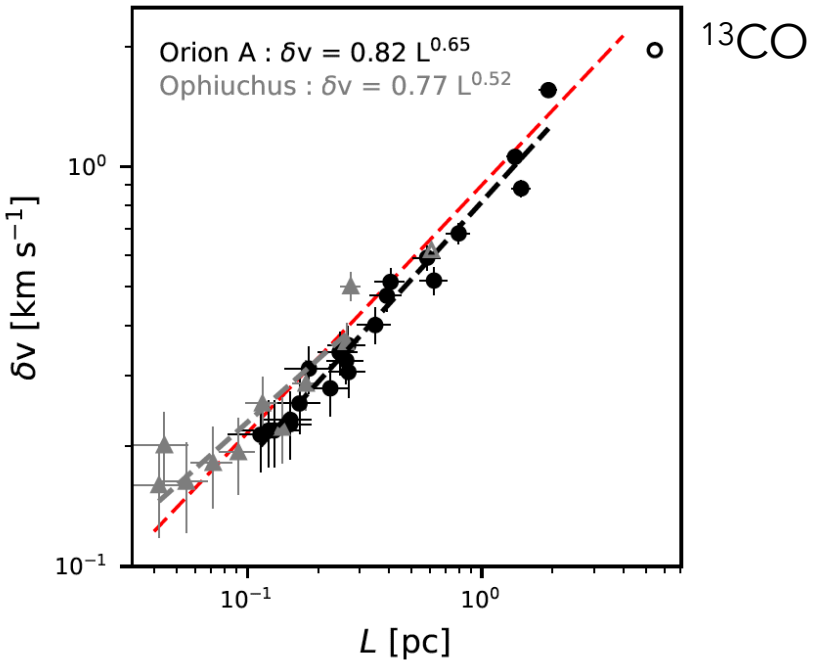

Cloud	N_{sig}	p_{var}	$\log_{10}(\delta v_0)$	α
Orion A	22	72.1	-0.09±0.02	0.65±0.05
Ophiuchus	12	90.3	-0.12±0.13	0.52±0.14

2次の速度構造関数 $\sqrt{\langle v_l^2 \rangle} \propto l^{\gamma}$
ベストフィットに対するγは
Orion A, Ophiuchusそれぞれ 0.56 and 0.34

クラウドをいくつかの領域に分割 (sub-regionごとに異なる距離を採用)

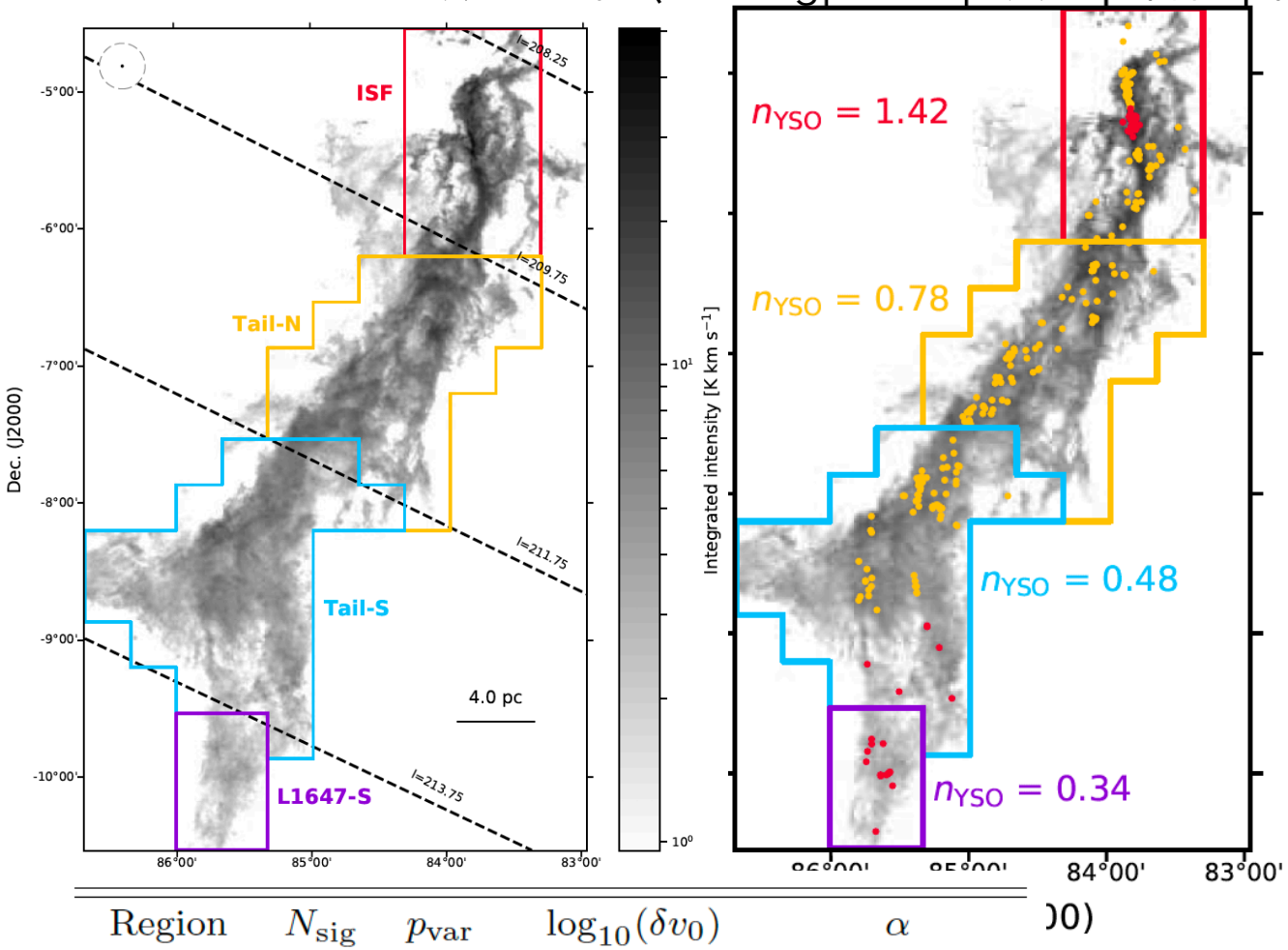

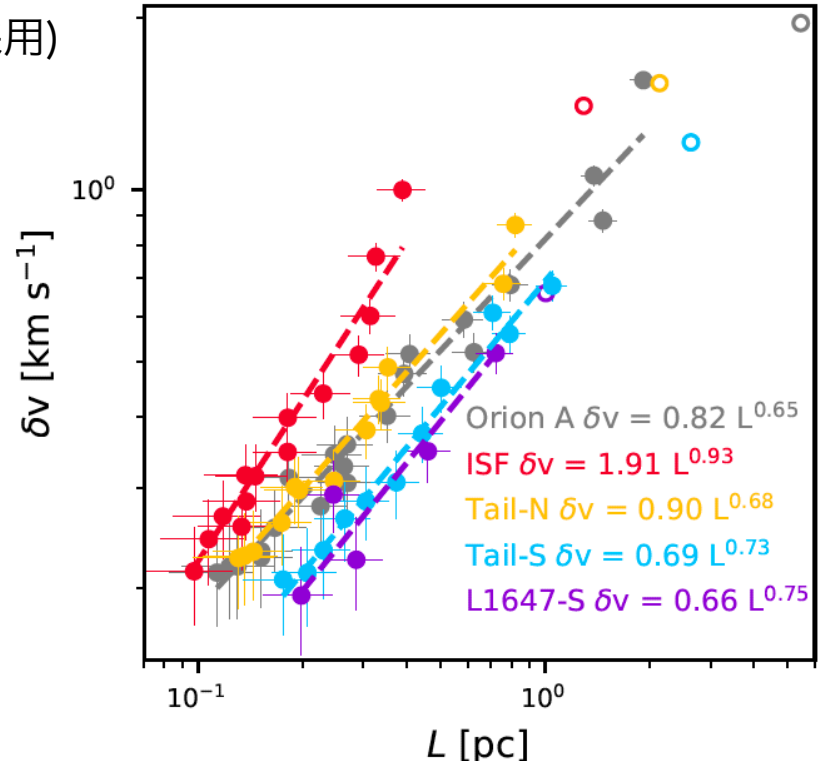

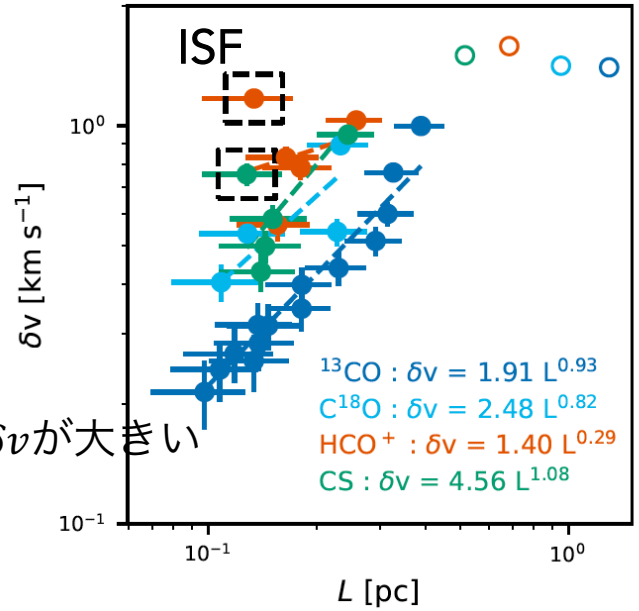

Region	N_{sig}	p_{var}	$\log_{10}(\delta v_0)$	α
In the Orion A cloud				
ISF	16	84.3	0.282±0.124	0.933±0.182
Tail-N	15	75.5	-0.047±0.046	0.684±0.096
Tail-S	13	63.8	-0.161±0.037	0.731±0.112
L1647-S	7	35.4	-0.181±0.103	0.747±0.249

星形成活動が活発な北側の方が
δvもαも大きい

13COよりC^{18}O, HCO$^+$, CSの方がδvが大きい
→高密度ガスの方がより乱れた状態

クラウドをいくつかの領域に分割
(距離はsub-regionごとに異なる)

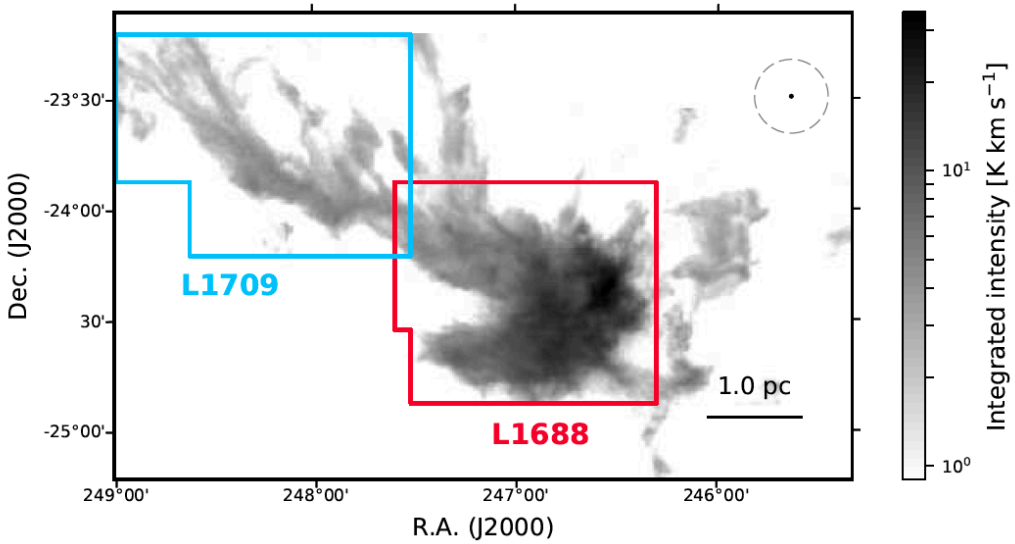

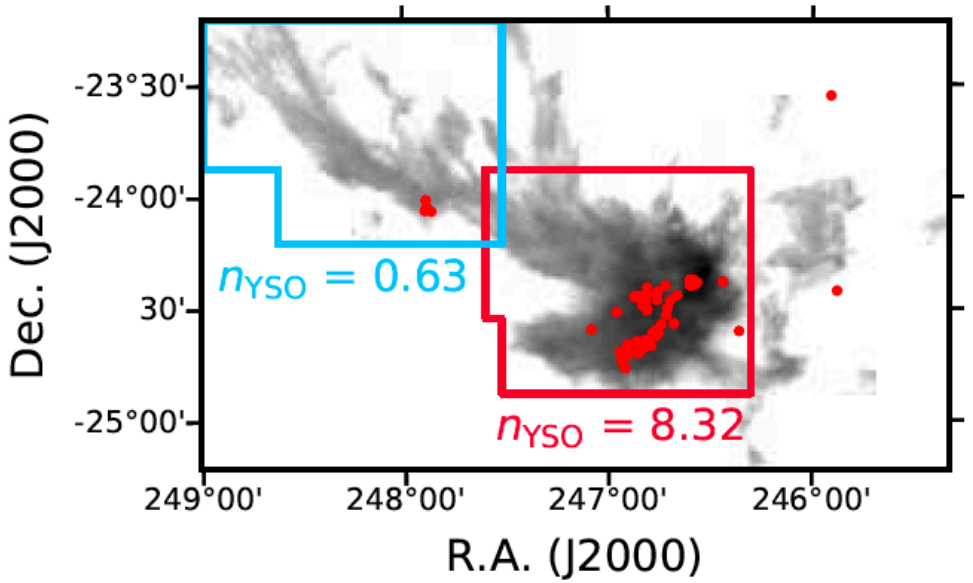

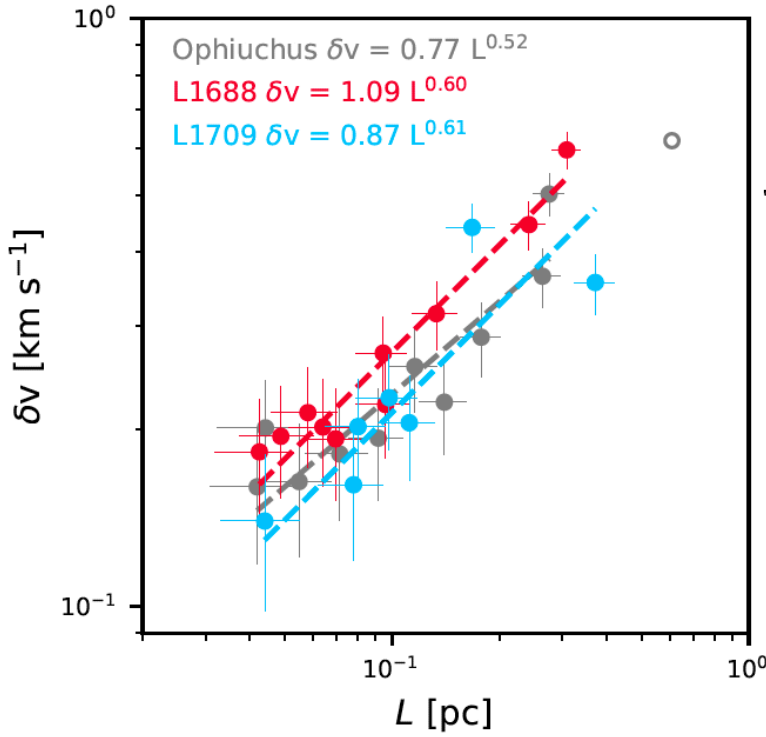

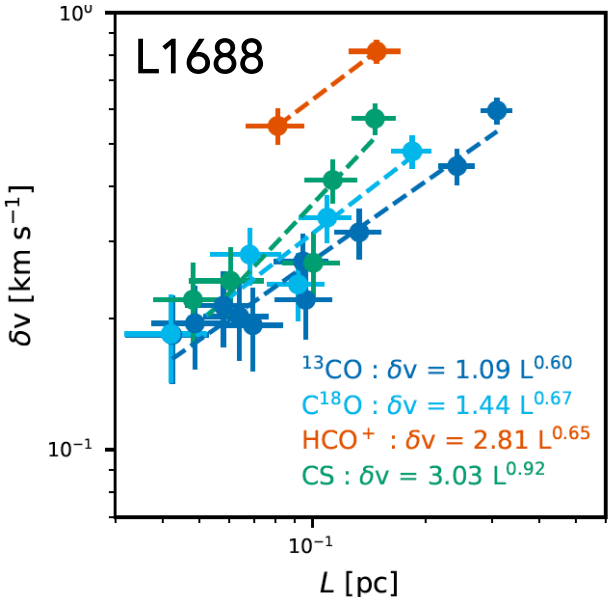

Region	N_{sig}	p_{var}	$\log_{10}(\delta v_0)$	α
In the Ophiuchus cloud				
L1688	11	96.5	0.036±0.097	0.604±0.109
L1709	8	72.6	-0.062±0.191	0.609±0.219

星形成活動が活発なL1688の方が
δvもαも大きい

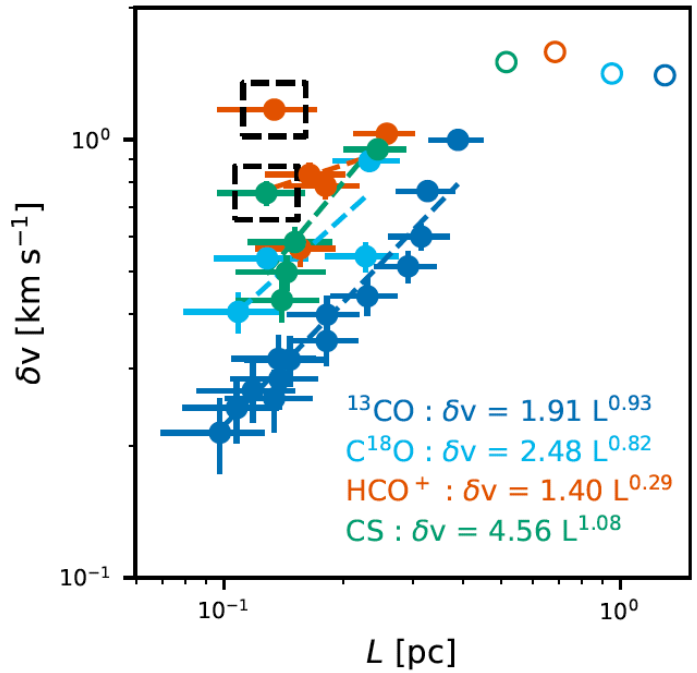

Orion KL outflow
の影響を除去

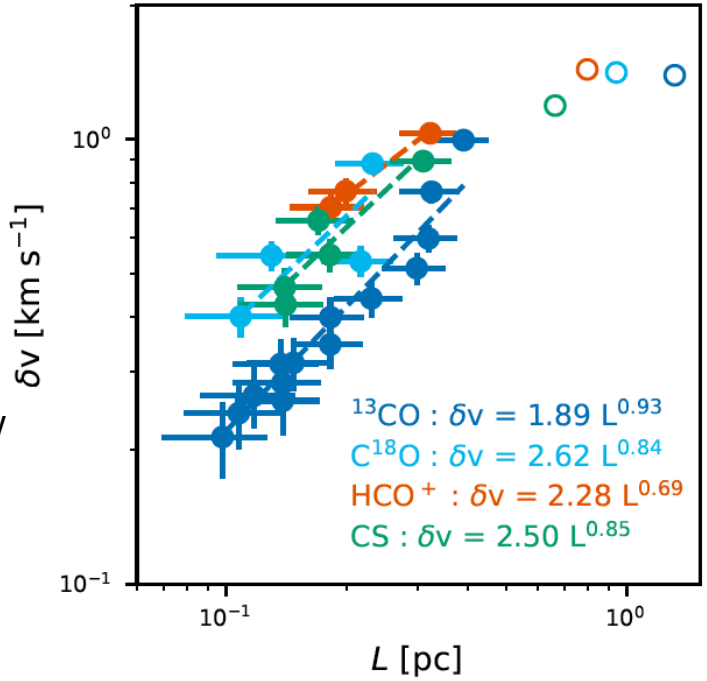

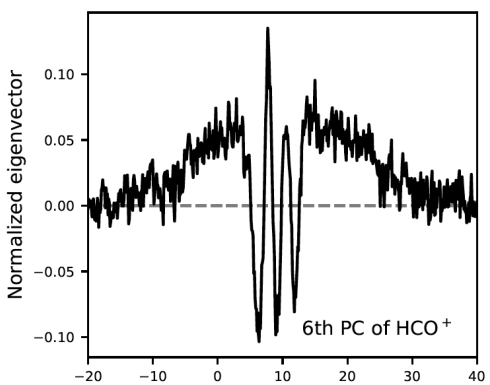

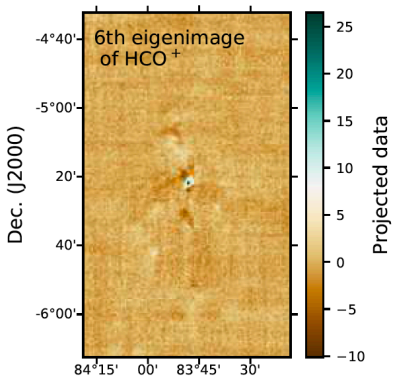

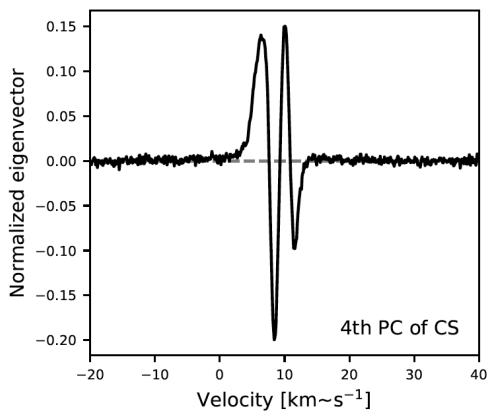

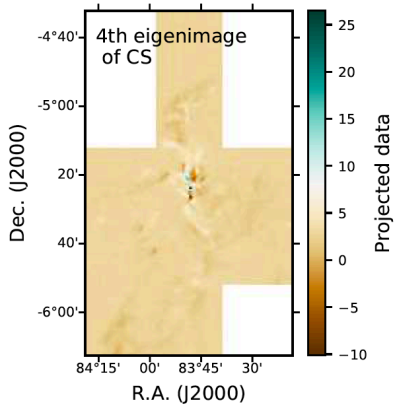

Orion KL outflowによるδvの増大

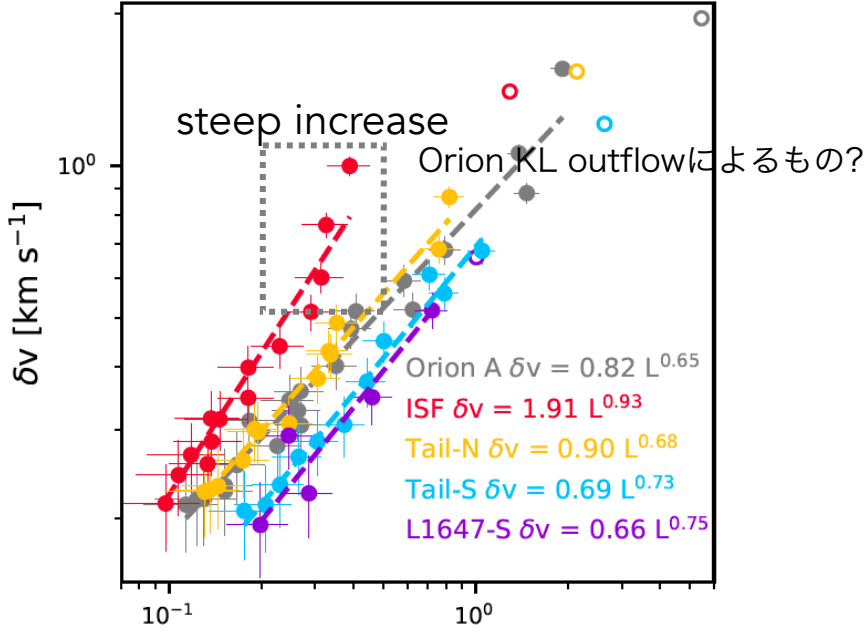

HCO+が検出されたinner regionを除外した場合
steep increaseは未だ存在

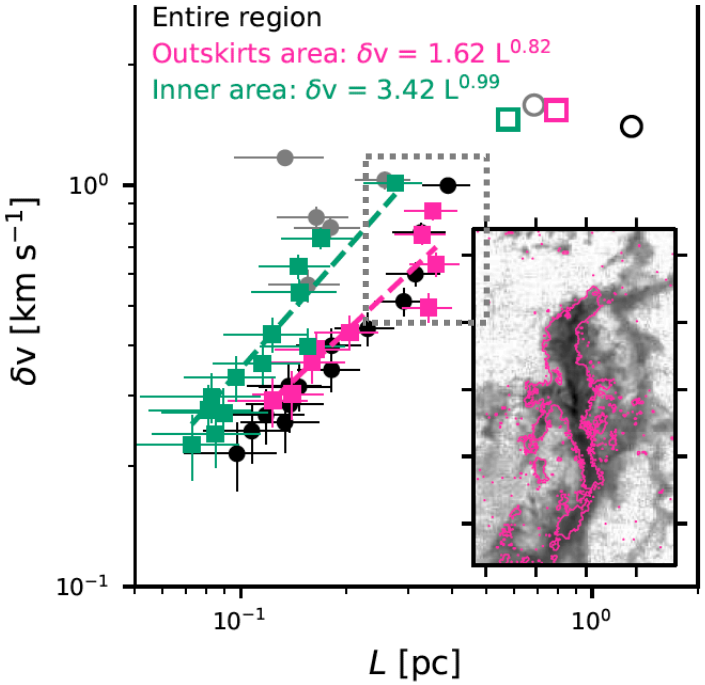

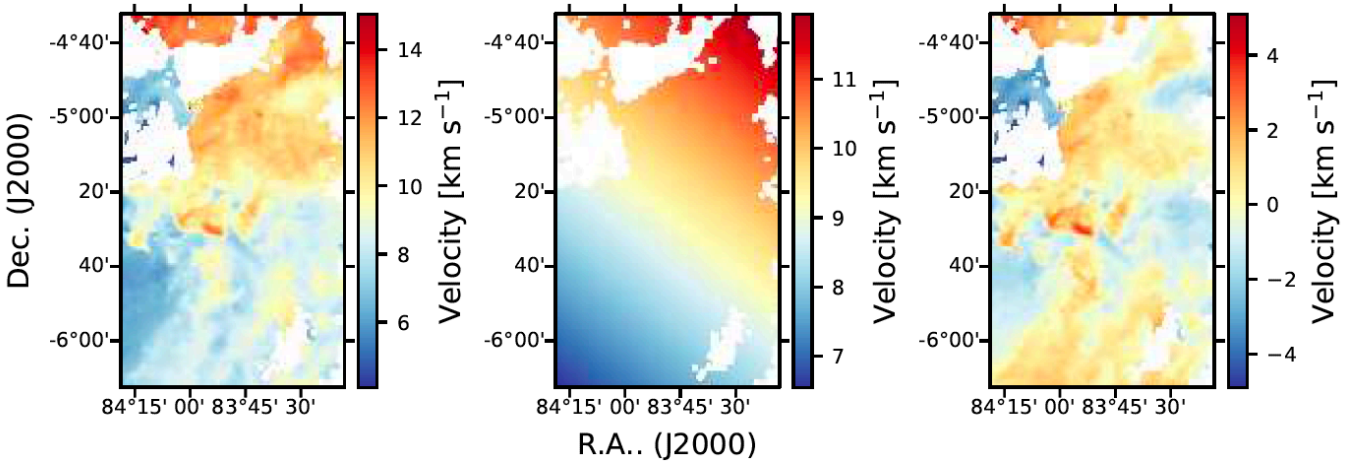

large-scale motionを考慮した場合
steep increaseがなくなった
→局所的な星形成活動ではなくlarge motionによるもの

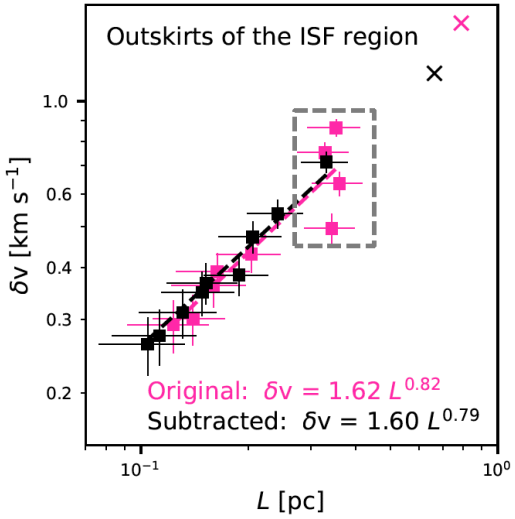

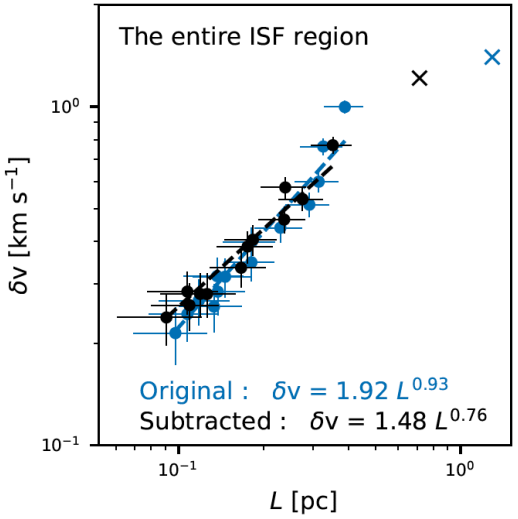

18. An orbital release model for the Orion BN/KL fingers

A. C. Raga, P. R. Rivera-Ortiz, A. Rodriguez-Gonzalez, A. Castellanos-Ramirez

We present a simple model in which the bullets that produce the "Orion fingers" (ejected by the BN/KL object) are interpreted as protoplanets or low mass protostars in orbit around a high mass star that has a supernova explosion. As the remnant of the SN explosion has only a small fraction of the mass of the pre-supernova star, the orbiting objects then move away in free trajectories, preserving their orbital velocity at the time of release. We show that a system of objects arranged in approximately co-planar orbits results in trajectories with morphological and kinematical characteristics resembling the Orion fingers. We show that, under the assumption of constant velocity motions, the positions of the observed heads of the fingers can be used to reconstruct the properties of the orbital structure from which they originated, resulting in a compact disk with an outer radius of ~ 2.4 AU.

Orion fingersを形成するbulletsが超新星爆発を伴う大質量星周りの軌道にある原始惑星や小質量原始星であるというモデル

ほぼ同一平面上の軌道に配置された天体がOrion fingersに形態的にも力学的にも似た軌道になることを示した

head of the fingersの観測結果からfingerが形成された軌道特性を再現した結果, outer radius ~2.4 auの円盤

20. Optical Properties of Interstellar Dust around the Orion A Molecular Cloud

Hayato Uehara, Kazuhito Dobashi, Shingo Nishiura, Tomomi Shimoikura, Takahiro Naoi

We have studied optical properties of interstellar dust around the Orion A molecular cloud to investigate the size distribution and the composition of dust grains. Orion A is one of the most studied molecular clouds in the solar vicinity ($d \simeq 400$ pc). In this paper, we used optical and near-infrared photometric data. The optical data were obtained by $BVRI$ bands imaging observations. The near-infrared data consisting of JHK_S bands were taken from 2MASS point source catalog. We produced some color excess maps around Orion A, and measured their ratios such as $E(R-I)/E(B-V)$. In order to investigate dust properties, we compared the observed ratios with results of simulation performed by Naoi T. et al. (2021) who calculated the extinction in the optical to near-infrared wavelengths based on a standard dust model; they assumed a power-law grain-size distribution with an upper cutoff radius and assumed *graphite* and *silicate* as dominant components. As a result, we found that the upper cutoff radius around Orion A is $\simeq 0.3$ μm, and *silicate* predominates compared with *graphite* (with the fraction of *silicate* grater than 93 %). In addition, we further derived the total-to-selective extinction ratio R_V from the observed extinction of A_V and the color excess $E(B-V)$, and compared it with the model calculations. Dust properties (i.e., the upper cutoff radius and the ratio of *graphite*/*silicate*) derived from R_V is almost consistent with those derived from the color excess ratios.

Orion A分子雲周りの星間ダストの光学特性

可視光データ BVRIバンド近赤外データ JHKsバンド (2MASS point source catalog)

E(R-I)/E(B-V) 観測とシミュレーションを比較→ダスト半径の上限(upper cutoff)~0.3 μm, silicate > 93%

観測で得られたAvとE(B-V)からRvを見積もりモデル計算と比較→ほぼ一致

色超過比とNaoi et al. (2021)で計算されたダストサイズ分布の
upper cutoff radiusの関係

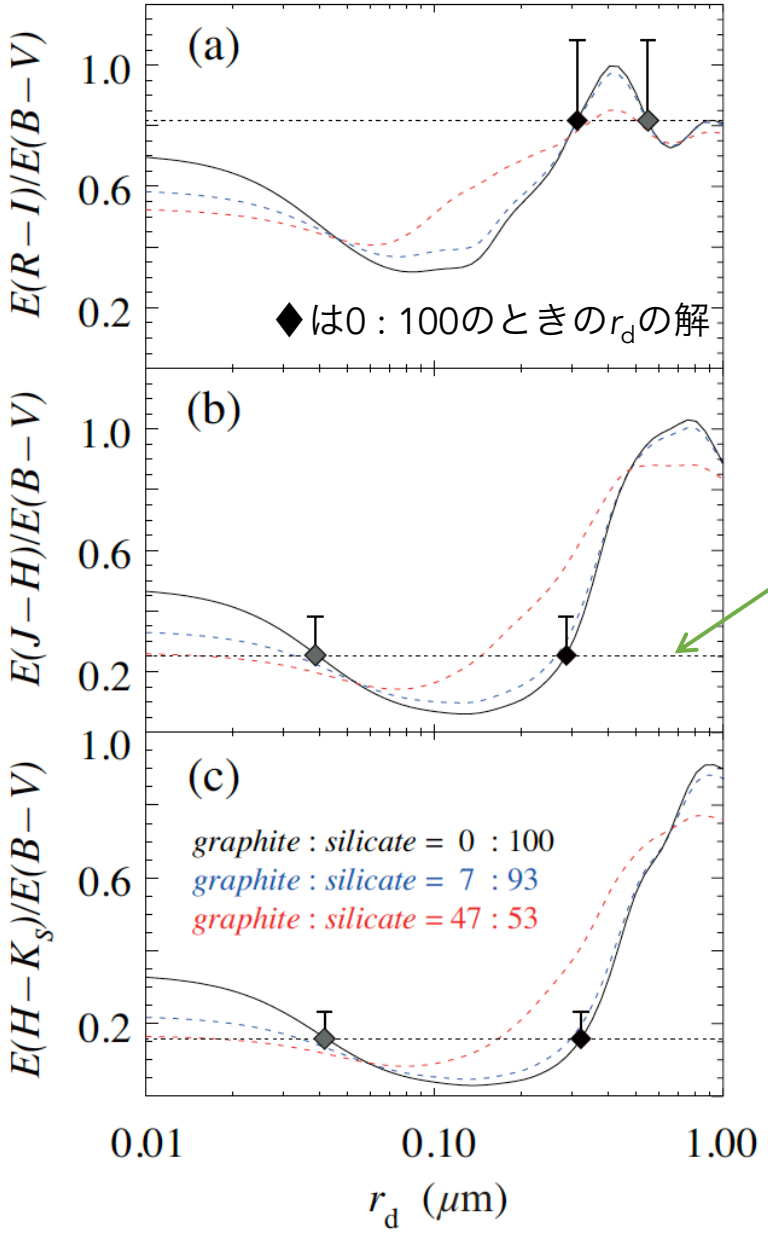

the upper cutoff radius of the size distribution

Table 3. Color Excess Ratios Obtained by the Ordinary Least Squares Method

Color Excess Ratio	Slope $a_1 \pm \sigma_{a_1}$	Intercept $a_0 \pm \sigma_{a_0}$
$E(R-I)/E(B-V)$	0.817 ± 0.0052	-0.040 ± 0.0020
$E(J-H)/E(B-V)$	0.253 ± 0.0057	-0.0003 ± 0.0025
$E(H-K_S)/E(B-V)$	0.144 ± 0.0045	0.0009 ± 0.0019

NOTE—The values of a_0 and a_1 are obtained by the Ordinary Least Squares (OLS) method, and they correspond to those in Figure 8.

Table 5. Upper Cutoff Radius r_d of Dust Size Distribution

Combinations of Color Excess	Range of Upper Cutoff Radius: Lower r_d (μm)	Higher r_d (μm)
$E(R-I)/E(B-V)$	0.312 – 0.402	(0.415 – 0.549)
$E(J-H)/E(B-V)$	(0.023 – 0.039)	0.263 – 0.328
$E(H-K_S)/E(B-V)$	(0.011 – 0.045)	0.282 – 0.354

NOTE—Ranges of r_d which vary depending on the fraction of *silicate* (for the range $93\% - 100\%$) and the values of a_1 (Tables 3 and 4) are summarized. For a given set of the fraction of *silicate* and a_1, there are two solutions in r_d (Figure 9), as they are indicated as "Lower r_d" and "Higher r_d" in the table. Ranges of r_d in the parentheses are false solutions (see text).

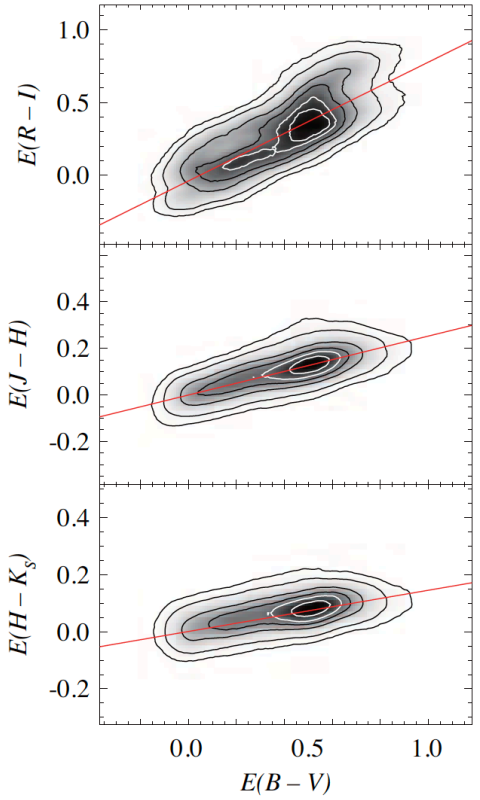

21. Probing Protoplanetary Disk Winds with C II Absorption

Ziyan Xu, Gregory J. Herczeg, Christopher M. Johns-Krull, Kevin France

We present an analysis of wind absorption in the C II λ1335 doublet towards 40 classical T Tauri stars with archival far-ultraviolet (FUV) spectra obtained by the Hubble Space Telescope. Absorption features produced by fast or slow winds are commonly detected (36 out of 40 targets) in our sample. The wind velocity of the fast wind decreases with disk inclination, consistent with expectations for a collimated jet. Slow wind absorption is detected mostly in disks with intermediate or high inclination, without a significant dependence of wind velocity on disk inclination. Both the fast and slow wind absorption are preferentially detected in FUV lines of neutral or singly ionized atoms. The Mg II λλ2796, 2804 lines show wind absorption consistent with the absorption in the C II lines. We develop simplified semi-analytical disk/wind models to interpret the observational disk wind absorption. Both fast and slow winds are consistent with expectations from a thermal-magnetized disk wind model and are generally inconsistent with a purely thermal wind. Both the models and the observational analysis indicate that wind absorption occurs preferentially from the inner disk, offering a wind diagnostic in complement to optical forbidden line emission that traces the wind in larger volumes.

fast/slow wind由来のC Ⅱ λ1335吸収線をT Tauri stars 36/40で検出

diskの傾きが大きいほどwindの速度は遅くなる傾向あり(collimated jetで予想されるものと一致)

観測プロファイルはpure thermal windではなくthermal-magnetized wind のdisk-wind 解析モデルと一致

モデルと観測はinner diskからwindの吸収が生じていることを示唆

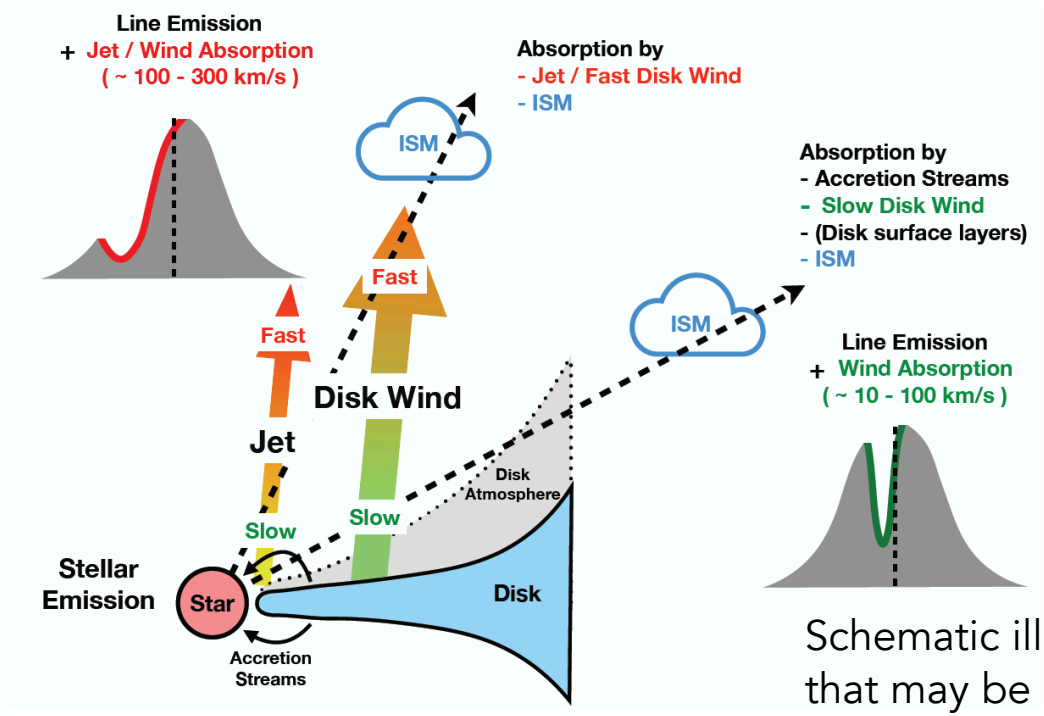

Schematic illustration of the absorption components
that may be detected depending on our viewing angle of the star-disk system

CII λ1335 line proles

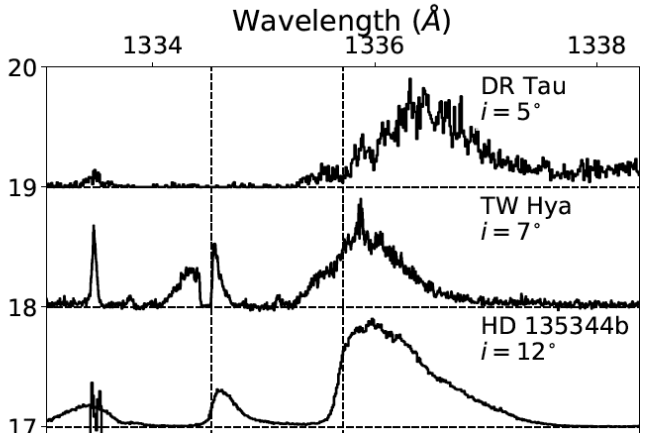

fast wind absorptions

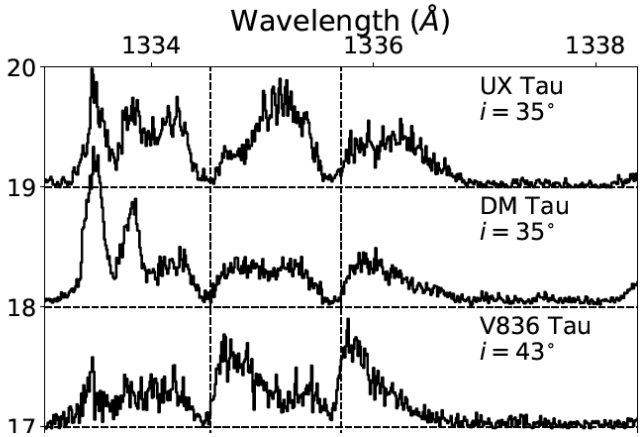

slow wind absorptions

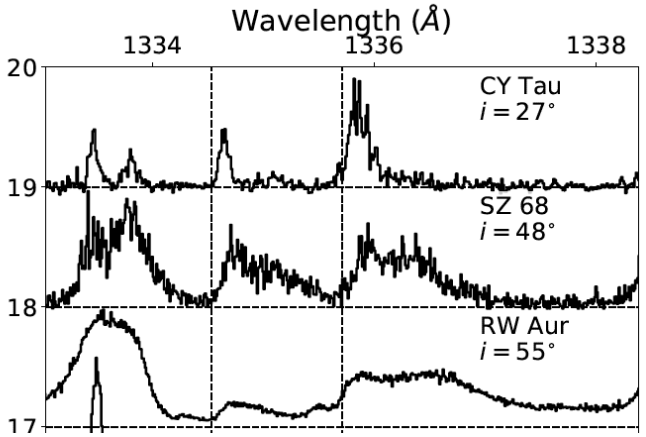

no clear wind absorptions

Kaho.M 2021/09/10 #344 18-22